JOURNAL OF GEOPHYSICAL RESEARCH, VOL. 105, NO. B12, PAGES 28,363–28,376, DECEMBER 10, 2000

Strain partitioning during oblique plate convergence in northern Sumatra: Geodetic and seismologic constraints and numerical modeling

Robert McCaffrey,[1] Peter C. Zwick,[1] Yehuda Bock,[2] Linette Prawirodirdjo,[2]
Joachim F. Genrich,[2] Colleen W. Stevens,[1] S. S. O. Puntodewo,[3]
and Cecep Subarya[3]

Abstract. Global Positioning System (GPS) measurements along the subduction zone of northern Sumatra (2°S to 3°N) reveal that the strain associated with the oblique convergence of the Australian plate with Eurasia is almost fully partitioned between trench-normal contraction within the forearc and trench-parallel shear strain within a few tens of kilometers of the Sumatran fault. Kinematic analyses of interplate earthquake slip vectors provide slip rates on the Sumatran fault within a few millimeters per year of GPS and geologic rates, giving us more confidence in the use of slip vectors for inferring slip partitioning elsewhere. The inferred slip rate on the Sumatran fault is ~1/3 less than the full margin parallel component of plate motion. An across-forearc rotation in the slip vectors suggests that the missing arc-parallel shear occurs seaward of the geodetic network, between the forearc islands and the trench. Simple finite element models are used to explore the conditions under which the change in the principal strain rate directions between the forearc and the arc region can occur. Modeling suggests that neither a preexisting strike-slip fault nor a zone of thermally induced lithospheric weakness in the overriding plate is needed for strain partitioning to occur. In general, forearc slivers form over the region of interplate coupling and are driven along strike by the basal shear. A volcanic arc can help the partitioning process by localizing the margin-parallel shear strain in the upper plate if its crust and mantle are weaker than its surroundings. Interplate slip vectors and geodetic results from Sumatra together suggest that the highest coupling on the plate boundary occurs beneath and seaward of the forearc islands, consistent with inferences about the rupture zones of great nineteenth century earthquakes there. The Sumatra example suggests that geodetic measurements of interseismic, margin-parallel shear strain at oblique convergent margins can be used to map the landward extent of the relatively high basal stress beneath the overriding plate if one can correct for strain localization caused by weak upper plate strike-slip faults.

1. Introduction

Owing largely to the early work of *Fitch* [1972], the accommodation of the oblique convergence between the Australian and Eurasian plates at Sumatra has long been cited as the type example of slip partitioning along a subduction zone. During slip partitioning, the oblique convergence between two plates occurs on two separate, usually parallel, faults. Some or all of the margin-parallel component of relative motion occurs on a strike-slip fault, while all of the convergence and the remaining shear occur on a dipping thrust fault. Since that first description of slip partitioning, it has been observed at numerous subduction zones and convergent margins [e.g., *Jarrard*, 1986; *McCaffrey*, 1994]. The mechanics of the slip partitioning at subduction zones are fairly well understood for very simple Earth models [*Beck*, 1983; *Avé Lallemant and Guth*, 1990; *McCaffrey*, 1992; *Platt*, 1993] that were adequate in the past given the type of data that were available to study the process. Specifically, information such as fault slip rates and the deflection of subduction thrust earthquake slip vectors reveal the large scale block motions but they are not particularly sensitive to short-term strains and their spatial variations that occur during oblique convergence. Because oblique convergence includes a component of interplate force that is parallel to the trend of the margin, it provides a means to study subduction dynamics that has not been exploited in two-dimensional models. Moreover, modern geodetic techniques can reveal spatial strain variations that should accompany oblique subduction [*Walcott*, 1978; *Savage and Lisowski*, 1988].

Inferences of slip partitioning were made initially from the rotation of subduction zone thrust earthquake slip vectors away from the plate convergence vector and toward the trench-normal direction [*Fitch*, 1972; *Jarrard*, 1986]. Such slip vector rotation is best explained by arc-parallel translation of the forearc in response to the arc-parallel stresses of oblique subduction. At some subduction zones, along-strike forearc stretching is also required to explain the changes in slip vector orientations [*Ekström and*

[1] Department of Earth and Environmental Sciences, Rensselaer Polytechnic Institute, Troy, New York.
[2] Institute of Geophysics and Planetary Physics, Scripps Institution of Oceanography, La Jolla, California.
[3] National Coordination Agency for Surveying and Mapping, Cibinong, Indonesia.

Paper number 1999JB900362.
0148-0227/00/1999JB900362$09.00

Engdahl, 1989; *McCaffrey,* 1991, 1992]. At several of these forearcs, stretching has been confirmed by geologic and geodetic observations (see *McCaffrey* [1996a] for a summary). Despite the general practice of using interplate slip vectors to infer forearc kinematics and slip partitioning, the relationship between the slip vectors and partitioning has not been directly demonstrated, leading to some suggestions that the slip vector deflections arise from other causes, for example, from deformation of the subducting plate [*Liu et al.*, 1995; *Lallemand and Chemenda*, 1999]. Here we show that the kinematic inferences derived from slip vectors in northern Sumatra are entirely consistent with the upper plate velocity and strain fields measured directly with geodetic methods.

Strain partitioning at oblique subduction zones might also be used to reveal some details of the stresses acting on the dipping plate boundary. For example, *Savage* [1983] suggested that in oblique subduction zones the downdip end of the plate coupling zone should give rise to elastic shear strain in the overriding plate very similar to the effects of a buried, trench-parallel strike-slip fault. The Savage dislocation model and geodetic observations of margin-parallel shear strain were subsequently used to infer the landward extent of plate coupling in southern Alaska [*Savage and Lisowski*, 1988; *Sauber et al.*, 1997]. However, an opposing viewpoint holds that the location of the upper plate shear strain is controlled by a zone of shear weakness in the overriding plate, a volcanic arc, for example [*Beck*, 1983], and provides little information about interplate stress. Still a third possibility, a combination of the two previous cases, is that the stress distribution on the plate boundary thrust fault leads to strain localization and formation of an upper plate strike-slip fault. If stress on the thrust fault changes subsequently, the upper plate fault may continue to localize the shear strain and the information about stress is lost. The distinction between the two types of upper plate strain can be made on the basis of whether the strain is elastic and recovered during plate boundary earthquakes or permanent and evident in upper plate faults. Geodetic measurements by themselves made over decade timescales often cannot distinguish elastic from permanent strains, and other indicators must also be used.

Global Positioning System (GPS) campaigns were initiated in the northern Sumatra region in 1989 and were conducted annually until 1995 to explore the mechanics of strain partitioning at an oblique subduction zone [*Bock et al.*, 1990; *McCaffrey et al.*, 1990]. In this paper, we utilize strain rates estimated from the GPS measurements along with finite element modeling to explore the factors that control strain partitioning and also to elucidate what details of the subduction process we can learn from such geodetic measurements in obliquely convergent margins. Details of the field work and data analysis in Sumatra are given by *Genrich et al.* [this issue] who also model variations in slip rates on the Sumatran fault in northern Sumatra and by *Prawirodirdjo et al.* [this issue] who examine crustal deformation in Sumatra over the last 100 years from a combination of historical triangulation and GPS measurements.

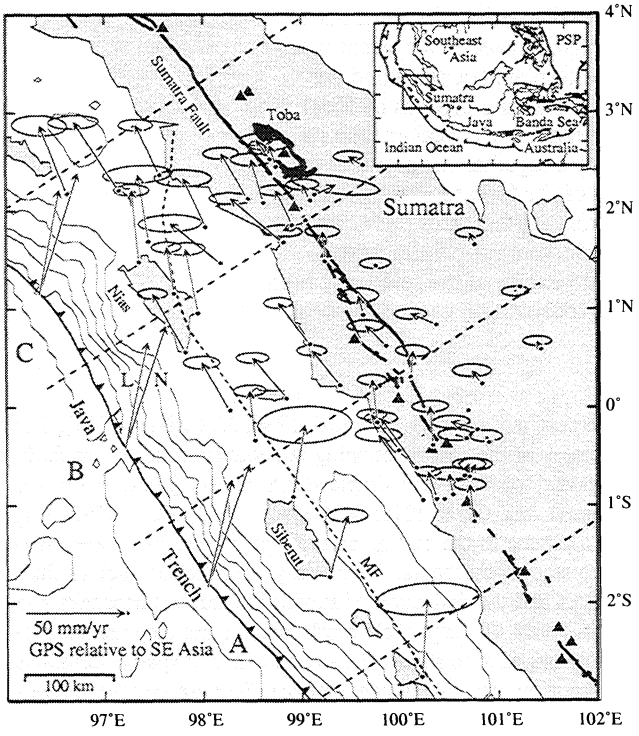

Figure 1. GPS-derived velocity vectors with 95% confidence ellipses relative to eastern Sumatra (SE Asia). Scale shown at lower left. Arrows at trench are plate convergence vectors, the more northerly of each pair (labeled L) are from the Australia-Eurasia pole of *Larson et al.* [1997] and those labeled N are from the NUVEL-1A Australia-Eurasia pole of *DeMets et al.* [1994]. NE trending dashed lines show boundaries of the subduction zone segments labeled A, B, and C discussed in the text. Triangles show locations of active volcanoes. Bathymetric interval is 1000 m. Dashed line labeled MF is the trace of the inferred Mentawi fault [*Diament et al.*, 1992]. Box in inset shows study region. PSP, Philippine Sea plate.

2. Strain Rate Tensors at Sumatra from GPS Measurements

GPS vectors in Figure 1 are shown in the Eurasian reference frame in which the back arc region is essentially fixed. However, the reference frame is not important here because we are interested primarily in the strain rates that derive from the gradients in the velocities. The area spanned by the GPS network is divided into seven regions of roughly 150 km by 200 km each (Figure 2). A deformation rate gradient tensor, rotation rate, and strain rate tensor are calculated for each region (Table 1). The regions are overlapped to improve estimates of strain rates at the expense of resolution of their spatial variations. The SW coast of Sumatra was taken as a boundary between regions because it coincides with the landward extent of seismic activity on the thrust fault, as shown by the distribution of interplate earthquake slip vectors (Figure 2).

To estimate two-dimensional (surface) infinitesimal strain rate tensors from the horizontal components (x=east, y=north) of the estimated GPS-derived velocities, the velocity field $\mathbf{V}(x,y)$ is decomposed as follows:

$$\mathbf{V}(x,y) = \mathbf{L}\,\mathbf{X} + \mathbf{T} + \mathbf{E}(\mathbf{X}) \tag{1}$$

where $\mathbf{L}$ is the deformation rate gradient tensor.

$$\mathbf{L} = \begin{vmatrix} \partial V_x/\partial x & \partial V_x/\partial y \\ \partial V_y/\partial x & \partial V_y/\partial y \end{vmatrix}. \tag{2}$$

$\mathbf{X}$ is a position vector, $\mathbf{T}$ is a position independent translation vector (T_x, T_y), and $\mathbf{E}(\mathbf{X})$ is an error vector. Written out in its components the velocity field is

Table 1. Strain Rates and Deformation Gradients

Region	$\dot{\varepsilon}_{11}$	Azimuth of $\dot{\varepsilon}_{11}$, deg	$\dot{\varepsilon}_{22}$	Rotation Rate	N	χ^2	L_{xx}	L_{xy}	L_{yx}	L_{yy}
1	-0.16 ± 0.09	58 ± 11	0.00 ± 0.06	0.02 ± 0.07	8	2.8	-0.11 ± 0.09	-0.06 ± 0.07	-0.09 ± 0.03	-0.04 ± 0.02
2	-0.06 ± 0.09	55 ± 11	0.06 ± 0.07	0.02 ± 0.09	7	0.4	-0.02 ± 0.06	-0.04 ± 0.08	-0.08 ± 0.02	0.02 ± 0.02
3	-0.14 ± 0.14	48 ± 11	0.08 ± 0.08	0.02 ± 0.10	8	0.9	-0.04 ± 0.12	-0.09 ± 0.09	-0.13 ± 0.04	-0.02 ± 0.03
4	-0.10 ± 0.04	25 ± 11	0.09 ± 0.07	0.10 ± 0.06	16	2.1	0.06 ± 0.07	0.02 ± 0.06	-0.17 ± 0.02	-0.07 ± 0.02
5	-0.09 ± 0.03	13 ± 10	0.09 ± 0.06	0.08 ± 0.05	11	3.1	0.08 ± 0.06	0.04 ± 0.05	-0.12 ± 0.02	-0.08 ± 0.01
6	-0.15 ± 0.09	12 ± 12	0.17 ± 0.17	0.25 ± 0.14	9	2.6	0.15 ± 0.17	0.19 ± 0.14	-0.32 ± 0.05	-0.14 ± 0.04
7	-0.01 ± 0.03	168 ± 13	0.02 ± 0.08	0.02 ± 0.05	8	1.1	0.02 ± 0.06	0.03 ± 0.04	-0.016 ± 0.02	-0.01 ± 0.01

The x axis in the deformation rate gradient tensor is east; the y axis is north. The 1 axis used in the principal strain rate tensor is in the direction of the maximum contraction. N is the number of GPS vectors in the region. χ^2 is the sum of the residuals divided by their individual standard deviations squared, then divided by the degrees of freedom, which is $2N$-6. Normal strain rates are in microstrain per year. Rotation and shear rates are in microradians per year.

$$V_x(\mathbf{X}) = (\partial V_x/\partial x)\ x + (\partial V_x/\partial y)\ y + T_x + E_x(\mathbf{X})$$

$$V_y(\mathbf{X}) = (\partial V_y/\partial x)\ x + (\partial V_y/\partial y)\ y + T_y + E_y(\mathbf{X}) \quad (3)$$

Using the observed values of V_x and V_y from the GPS observations, the components of **L** and **T** are estimated by weighted least squares (i.e., $\Sigma(E_x/f\sigma_x)^2$ and $\Sigma(E_y/f\sigma_y)^2$ are minimized),

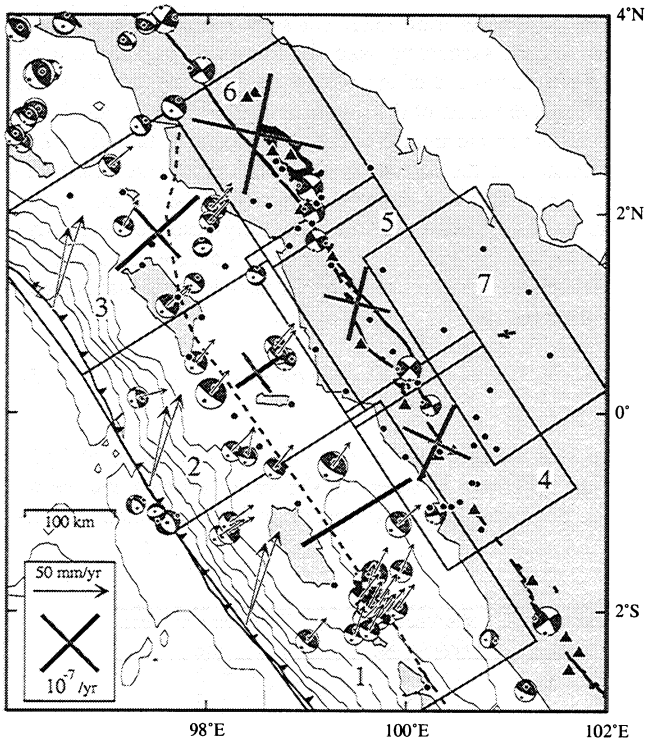

Figure 2. Fault plane solutions, slip vectors, and principal strain rates from GPS. Heavy solid lines show contraction and shaded lines show extensional principal strain rates derived from all GPS sites (large dots) within the boxes shown (strain rate scale at lower left). Small arrows emanating from the fault plane solutions show slip vectors of earthquakes due to the oceanic plate thrusting beneath the forearc. All earthquakes shown are shallower than 70 km depth; sources of quakes are given in text. Sizes of focal spheres are scaled to log of seismic moment, which range from 16.8 to 19.8. Arrows at trench show convergence vectors as in Figure 1, with scale at left. Triangles show locations of active volcanoes. Bathymetric interval is 1000 m. Dashed line is the trace of the inferred Mentawi fault [*Diament et al.*, 1992].

where σ_x and σ_y are the standard errors of the east and north velocity estimates, respectively. The estimated covariances between the horizontal velocity components are negligible (<0.1) and are ignored. The GPS-derived standard errors in velocities are multiplied by a factor f, here 3.0, to bring them in line with empirical uncertainty estimates from repeatabilities [e.g., *Feigl et al.*, 1993]. This factor produces an overall χ^2 misfit roughly equal to the number of degrees of freedom for forearc sites (regions 1-3, Table 1) where the strain is approximately uniform as assumed by (1) but, as expected, results in a larger χ^2 for land sites (regions 4-6) where the strain is not uniform.

The strain rate tensor $\dot{\varepsilon}$ is

$$\dot{\varepsilon} = \begin{vmatrix} \partial V_x/\partial x & \tfrac{1}{2}(\partial V_x/\partial y + \partial V_y/\partial x) \\ \tfrac{1}{2}(\partial V_y/\partial x + \partial V_x/\partial y) & \partial V_y/\partial y \end{vmatrix}, \quad (4)$$

and the rotation rate is $\dot{\theta} = \tfrac{1}{2}(\partial V_x/\partial y - \partial V_y/\partial x)$, where a positive value is clockwise rotation about a vertical axis looking down from above. The magnitudes and directions of principal strain rate components are estimated from the strain rate tensor. Formal uncertainties in the deformation rate gradients are used to estimate uncertainties in the strain rate tensor and rotation rate by propagation of errors. Uncertainties in the principal axes are estimated by Monte Carlo simulation.

Geodetic station positions (latitude and longitude) are converted to two-dimensional Cartesian coordinates using a Universal Transverse Mercator projection. East and north velocity components are used directly as V_x and V_y components, respectively. We tested the impact of this planar transformation on the estimated strain rates by calculating velocity vectors on a spherical Earth at the GPS sites using both near and distant poles of rotation that gave velocity magnitudes similar to the GPS rates shown in Figure 1. Strains and rotations were then calculated for the regions using these synthetic vectors. The correct rotation rates were recovered, and the strain rates, that should be zero, were of the order 0.001 μstrain/yr, i.e., considerably less than the uncertainties in strain rates derived from the GPS data. Hence the conversion to a planar system introduces no significant error in strain rates.

An important observational result is the change in the orientations of the principal strains between the forearc and the mainland (Figure 2 and Table 1). Within the forearc (regions 1-3), seaward of Sumatra's SW coastline, the contractional strain directions estimated from GPS are within 10° of being perpendicular to the trench, even though the convergence direction between the Australian plate and Sumatra (Eurasia) makes an angle of ~ 40° with the trench normal. The lack of long-term permanent vertical motions in the forearc suggests that this arc-perpendicular contraction is largely elastic strain accumulation

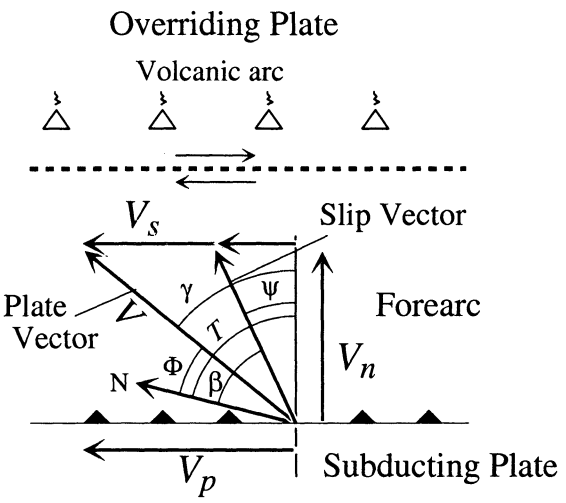

$$\gamma = T - \Phi \quad \psi = T - \beta$$
$$V_p = V \sin\gamma \quad V_n = V\cos\gamma$$
$$V_s = V(\sin\gamma - \cos\gamma\tan\psi)$$

Figure 3a. Diagram illustrating the relationship between the interplate earthquake slip vector, convergence vector V, and margin-parallel slip rate V_s. N is north, T is the azimuth of the normal to the trench, Φ is the plate convergence azimuth, β is the slip vector azimuth, γ is the plate convergence obliquity (the angle the convergence direction makes with the trench normal), and ψ is the slip vector obliquity (the angle the slip vector makes with the trench normal). V_p and V_n are the margin-parallel and margin-perpendicular components of the plate vector, respectively.

due to a temporal stress increase on the subduction thrust fault [*Prawirodirdjo et al.*, 1997; *Zachariasen et al.*, 1999].

The extensional strain rate in the forearc is directed parallel to the trench and is generally smaller than the contraction rate (though poorly determined). This extension is probably caused by subduction beneath the convex-seaward bend in the trench [*Avé Lallemant and Guth* 1990; *McCaffrey and Nabelek,* 1998]. The lack of extension in region 1 is consistent with uniform slip rates along the Sumatran fault adjacent to this section of the forearc [*Genrich et al.*, this issue; *Sieh and Natawidjaja*, this issue].

On the mainland and near the Sumatran fault the principal strain rate axes rotate by 30° to 40° anticlockwise relative to their orientations in the forearc, and the contractional and extensional strain rates become nearly equal in magnitude. The on-land principal strains indicate localized right-lateral shear strain parallel to the margin. The shear strain occurs only within ~25 km of the Sumatran fault and this width is likely due to elastic strain accumulation near the Sumatran fault [*Prawirodirdjo et al.*, 1997; *Genrich et al.*, this issue]. In region 7, the back arc, the strain rate is an order of magnitude smaller than elsewhere. These observations of spatial variations in strain will be used with numerical models to understand the causes of strain partitioning. Next, we compare the kinematics of the slip partitioning based on GPS and slip vectors.

3. Slip Vectors, GPS, and Slip Partitioning

Slip vectors of interplate thrust earthquakes can be used to estimate the rate of forearc translation and will be compared to direct measurements from GPS. Consider the three-plate system comprising the subducting plate, the forearc sliver, and the overriding plate landward of the volcanic arc (Figure 3a). Knowing the rate and direction of the subducting plate's motion relative to the overriding plate and the direction of motion of the subducting plate relative to the forearc from the interplate earthquake slip vectors and assuming a direction of motion of the forearc relative to the overriding plate, we can completely describe the relative motions of the three plates. Solving the three-plate velocity triangle (Figure 3a), the slip rate V_s on a strike-slip fault that is parallel to the trench is

$$V_s = V(\sin\gamma - \cos\gamma\tan\psi), \quad (5)$$

where V is the convergence rate, ψ is the slip vector obliquity (i.e., the difference between the slip vector azimuth and the direction perpendicular to the trench), and γ is the plate conver-

Table 2. Slip Vector Data

Segment	Trench Normal, deg	Rake Angle, deg	Dip Angle, deg	Number of Slip Vectors	Slip Vector Obliquity, deg	Slip Vector Azimuth, deg
A	54 ± 10	84 ± 26	14 ± 5	20	18 ± 15	36 ± 12
B	67 ± 6	86 ± 37	16 ±10	8	27 ±19	40 ± 17
C	53 ± 15	72 ± 37	19 ± 8	7	10 ± 17	43 ± 8

Segment	Plate Azimuth, deg	Plate Rate, mm/yr	Slip Vector Residual, deg	Plate Obliquity, deg	V_n, mm/yr	V_p, mm/yr	V_s, mm/yr	GPS Rate, mm/yr
			NUVEL-1A Australia - Eurasia Pole					
A	19 ± 1	66 ± 2	18 ± 12	35 ± 12	55 ± 5	38 ± 10	20 ± 3	23 ± 5
B	18 ± 1	65 ± 2	22 ± 17	49 ± 9	43 ± 4	49 ± 6	27 ± 7	24 ± 3
C	17 ± 1	64 ± 2	26 ± 8	36 ± 17	52 ± 8	38 ± 16	28 ± 1	25 ± 2
			Larson et al. Australia-Eurasia Pole					
A	13 ± 2	56 ± 3	24 ± 12	41 ± 12	42 ± 3	37 ± 10	23 ± 1	23 ± 5
B	12 ± 3	55 ± 3	29 ± 17	55 ± 9	31 ± 3	45 ± 7	29 ± 3	24 ± 3
C	10 ± 3	54 ± 3	33 ± 8	43 ± 17	39 ± 7	36 ± 14	29 ± 2	25 ± 2

V_n is plate motion rate normal to the trench, V_p is plate motion rate parallel to the trench, V_s is rate of forearc motion parallel to trench derived from slip vectors, GPS rate is the slip rate on the Sumatra fault derived from GPS measurements [*Genrich et al.*, this issue].

gence obliquity (i.e., the difference between the plate convergence azimuth and the direction perpendicular to the trench).

To estimate the rates of forearc translation and their uncertainties using slip vectors, we calculate means and standard deviations of azimuths of interplate thrust slip vectors, plate convergence vectors, and trench orientations (given by the normal to trench) within each of the arc segments A, B, and C shown in Figure 1 (Table 2). Slip vectors are taken from published first-motion and body waveform fault plane solutions for quakes prior to 1976 (citations listed by *McCaffrey* [1991]) and from the Harvard centroid moment tensor solutions from January 1976 through December 1998 [*Dziewonski et al.*, 1981; *Ekström and Nettles*, 1997]. We use slip vectors from earthquakes that are due to thrusting of the Australian plate beneath the forearc. The selection of earthquakes is based on location and depth of the quake, strike of the landward dipping plane, dip of the landward dipping plane, and rake angle. Plate convergence vectors are estimated from poles of rotation between the subducting Australian plate and the Sunda Shelf. For this we use two poles: (1) the NUVEL-1A Australia-Eurasia pole [*DeMets et al.*, 1994] assuming that the Sunda Shelf is part of Eurasia and (2) the Australia-Eurasia pole estimated from global GPS by *Larson et al.* [1997]. The Java trench outline is derived from the deepest points in the ETOPO5 seafloor database and smoothing with a polynomial [*McCaffrey*, 1994].

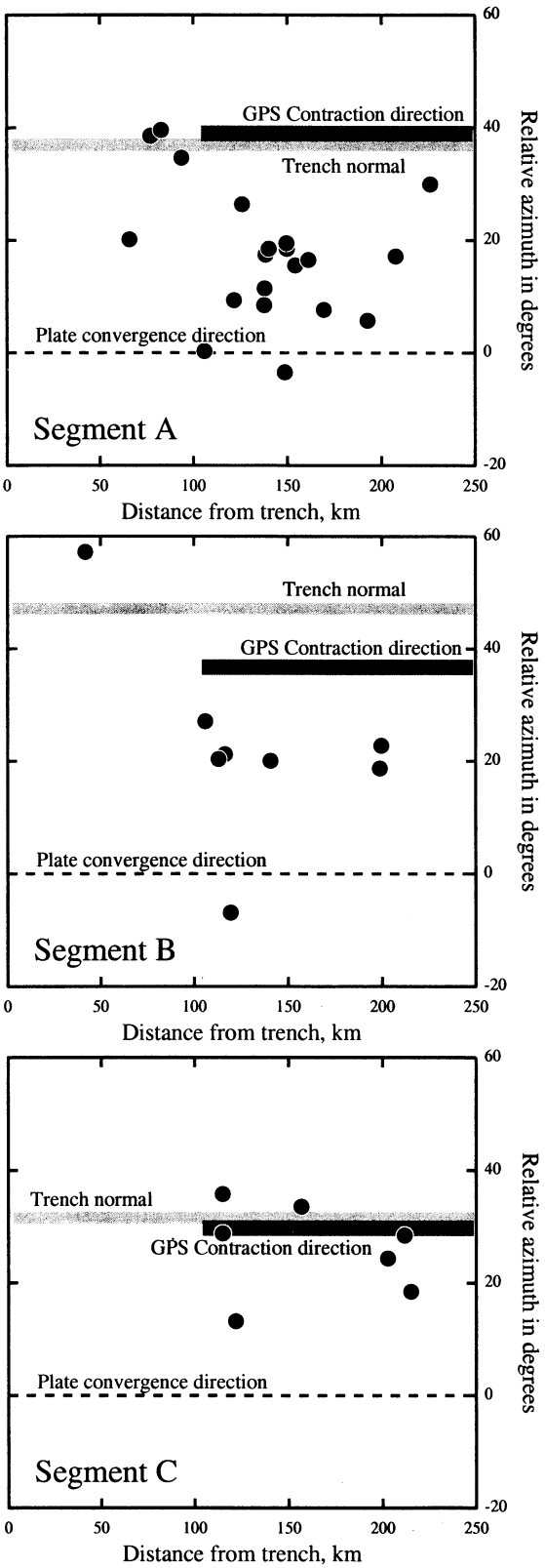

The average azimuths of earthquake slip vectors are rotated clockwise by ~20° relative to the plate convergence direction in all three regions (Figure 3b). However, it appears that, at least in segment A, slip vectors closest to the trench are nearly perpendicular to it and rotate across the forearc (Figures 2 and 3b). If the slip vectors are normal to the trench (i.e., $\psi \approx 0$), V_s approaches the full rate of trench-parallel plate motion given by $V \sin \gamma$. Hence the across-forearc rotation of the slip vectors may indicate some trench-parallel right-lateral shear between the trench and the outer coast of the forearc islands that might not be apparent in the GPS results (the across-forearc extent of the GPS network is shown by the darker shaded bars in Figure 3b).

Using (5) and data compiled for the arc segments (Table 2), calculated average arc-parallel slip rates range from 20 to 28 mm/yr using the NUVEL-1A pole and 23 to 29 mm/yr using the *Larson et al.* [1997] GPS-based pole (Table 2). For comparison, the Sumatra GPS measurements independently constrain slip rates on the Sumatran fault [*Genrich et al.*, this issue]. Two forearc-to-fault transects contained in segment A give 23±5 and 23±3 mm/yr, two in segment B give 23±4 and 24±2 mm/yr, and two in segment C show 24±1 and 26±2 mm/yr (Table 2). Hence estimates of Sumatran fault slip rates taken from deflections of slip vectors (using either pole) are all within 5 mm/yr of the estimates from GPS. The GPS and slip vector rates for the northern region also agree with a slip rate of 28 mm/yr inferred from stream channel offsets along the Sumatran fault near 2.2°N (in segment C) [*Sieh et al.*, 1994].

Figure 3b. Variations of slip vector azimuths across the forearc for the three forearc segments, plotted relative to the plate convergence azimuth. Dots show orientations of slip vectors. Lighter shaded bars show the azimuth of the trench normal relative to the plate convergence direction (the obliquity) and darker shaded bars show the direction of contraction in the forearc from GPS measurements. If no slip partitioning occurs, the slip vectors fall along the "plate" line, whereas during full partitioning, vectors fall along the "trench-normal" line. The decrease in the slip vector azimuths away from the trench, particularly for segment A, suggests that partitioning decreases landward, indicating a landward decrease in the margin-parallel velocity of the forearc.

The trench-parallel component of relative plate motion SW of Sumatra varies between 34 and 48 mm/yr depending on position along the trench and the pole of rotation used (Table 2). Geodetic, seismological, and geological measurements agree that in general ~60-70% of this motion is taken up by slip localized at the Sumatran fault in segments A and B. In segment C, the Sumatran fault takes up ~80% of it. The remaining 20-30% could be accommodated by strike-slip faults east of the Sumatran fault, by additional strike-slip faults in the forearc, or by oblique slip on the thrust interface. East of the Sumatran fault we see little indication of a shear zone in the GPS results, and none has been reported in the literature. Several GPS velocity profiles crossing the Mentawai Islands in the forearc, the Sumatran fault, and the back arc [*Genrich et al.*, this issue] allow an increase in the margin-parallel slip rate seaward of the Sumatran fault of at most 5 mm/yr, still short of the slip deficit in segments A and B. Beneath the geodetic array in the forearc of segments A and B, earthquake slip vectors show that there is sufficient oblique slip on the plate boundary to accommodate the remaining 1/3 of the margin-parallel motion. In segment C the slip vectors reveal much less obliquity, but the Sumatran fault also takes up a larger percentage of the margin-parallel slip. We conclude that the margin-parallel slip component in the forearc islands section of the forearc is accommodated fully by strike-slip on the Sumatran fault and by oblique slip on the thrust plate boundary below the islands.

Slip vectors in segments A and B, though sparse, suggest that convergence between the forearc and the subducting plate seaward of the GPS array might be nearly normal to the trench. Kinematically, this indicates that deformation in the leading edge of the forearc above where these earthquakes are occurring takes up all of the margin-parallel motion. Accordingly, slip vectors suggest that there may be an additional margin-parallel shear zone within the overriding plate between the SW coast of the forearc islands and the trench.

4. Finite Element Modeling of Oblique Subduction

We are interested in exploring the causes of the partitioning of slip and strain on separate, nearly parallel faults during oblique subduction. The GPS results from northern Sumatra indicate that trench-normal contractions occur largely in the forearc, while the trench-parallel shear strain is localized inboard of the forearc at the Sumatran fault. The Sumatran fault at present generally, though neither exclusively nor in detail, follows the line of active volcanoes [*Katili and Hehuwat*, 1967; *Page et al.*, 1979; *Sieh and Natawidjaja*, this issue]. Despite the lack of surface correlation between the fault and volcanic centers, it is possible that upper-plate shear strain is localized by a hot, weak zone in the hanging wall mantle. Following a global tendency, the Sumatran volcanic arc overlies the 100-125 km contour of the subducted slab [*Fauzi et al.*, 1996], so its geographic position is clearly determined by the slab and not by the presence of the Sumatran fault. However, few subduction zones have clear, well-developed strike-slip faults along volcanic arcs despite the ubiquity of volcanic arcs and convergence obliquity. Therefore we seek to understand the evolution of strain partitioning in oblique convergent systems and whether the arc-parallel strike-slip faults cause slip partitioning or result from it.

An observation that we think might be diagnostic is that the change in the pattern of strain in the forearc near the SW coast of Sumatra coincides with the downdip (landward) extent of interplate earthquakes (Figure 2). Accordingly, we will examine the possibility that the distribution of stress on the dipping, thrust plate boundary is a factor in controlling the pattern of strain partitioning in the overriding plate, as is inferred from dislocation models [*Savage*, 1983]. However, in dislocation models, Earth rheology is everywhere elastic and the resulting stresses are questionable [*Douglass and Buffett*, 1995]. We use a finite element model in which rheology can vary spatially and stress can be controlled. Understanding the relationship between strain partitioning and interplate stress can be useful in places where the downdip extent of possibly seismogenic interplate coupling cannot be measured seismologically but could be revealed in geodetic data.

We approach the problem of strain partitioning during oblique subduction by using a viscoelastic finite element model (FEM). Our main motivation is to examine whether or not the observed rotation of the principal strains in Sumatra can result from a simple model in which an oblique-slip thrust fault dips beneath the overriding plate. We use a modification of the FEM program

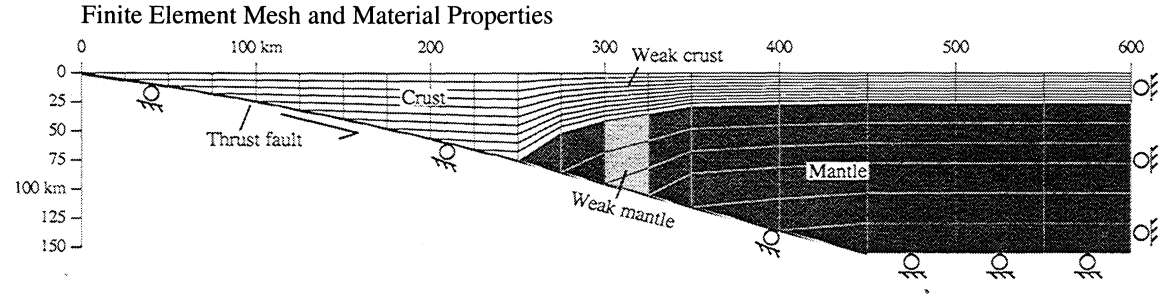

Figure 4. Cross section of 2-D mesh used in finite element modeling of oblique convergence in Sumatra. Models A through D use a simple two-layer structure comprising "crust" and "mantle". White region is crust of high effective viscosity (Tables 3 to 5). Dark region is the mantle and has moderately high effective viscosity in models A and B and lower effective viscosity in models C and D. Vertical column of shaded elements at x=300-325 km are assigned lower effective viscosities in models E and F to simulate a hot portion of the crust and mantle representing the "volcanic arc." The dipping boundary of the structure comprises 2-km thick elements that are assigned variable viscosities and high power law exponents (n = 5) to simulate plastic behavior along a dipping thrust fault. The bottom nodes of the dipping basal elements move with the convergence rate and include a component parallel to the margin to simulate oblique convergence. Material properties are given in Tables 3 to 5.

Table 3. Description of Finite Element Models

Model	Mantle	Coupling	Weak Zone
A	strong	deep	no
B	strong	shallow	no
C	weak	deep	no
D	weak	shallow	no
E	strong	deep	yes
F	strong	shallow	yes

Weak zone comprises "weak crust" and "weak mantle" as described in Table 4.

TECTON [*Melosh and Raefsky*, 1980] and model structure in two dimensions using a cross section perpendicular to strike of an infinitely long subduction zone (Figure 4). To allow oblique convergence, our implementation of the code, referred to as "2.5D", allows displacements and stresses in the along strike dimension. While there are numerous studies of subduction using finite elements, the reader is referred in particular to *Wang et al.* [1994], who use TECTON to model subduction in two-dimensions and give a nice overview of the impacts of various assumptions on the outcomes. *Taylor et al.* [1998] use a three-dimensional elastic model to focus on the impact of asperities on oblique subduction.

TECTON allows a range of viscoelastic materials with power law rheology using the constitutive equation

$$\dot{\varepsilon}_{ij} = 1/2\ \sigma_{\text{eff}}^{\,n-1}\ \sigma_{ij} / \eta_e^{\,n}, \tag{6}$$

where $\dot{\varepsilon}_{ij}$ is the strain rate tensor (units of s^{-1}), σ_{ij} is the stress tensor (in Pa),

$$\sigma_{\text{eff}} = (\tfrac{1}{2} (\sigma'^{\,2}_{11} + \sigma'^{\,2}_{22} + \sigma'^{\,2}_{33}) + \sigma^2_{12} + \sigma^2_{13} + \sigma^2_{23})^{1/2} \tag{7}$$

is the maximum effective shear stress (Pa), and σ'_{kk} is the mean deviatoric stress:

$$\sigma'_{kk} = \sigma_{kk} - 1/3\ (\sigma_{11} + \sigma_{22} + \sigma_{33}). \tag{8}$$

Maximum effective shear stress is the term used by *Patterson* [1981] for the second invariant of the deviatoric stress tensor, η_e is a user-specified coefficient related to viscosity, and n is the power law exponent. *Williams and Richardson* [1991] define a viscosity coefficient $\eta_c = \eta_e^{\,n}$ and a strain rate dependent effective viscosity

$$\eta_{\text{eff}} = \tfrac{1}{2}\ \dot{\varepsilon}^{\,(1/n-1)}\ (2\eta_c)^{\,1/n}. \tag{9}$$

Another useful measure of material behavior is the Maxwell time T_m. At times much less than T_m, elastic strain rates dominate the deformation, and at times much larger than T_m, viscous strain rates dominate.

Table 4. Parameters for Finite Element Models

Material	η_e, x 10^{10} (Pa s)$^{1/n}$	η_c, x 10^{34} (Pa s)^n	η_{eff}, x 10^{19} (Pa s)	T_m, years
Strong crust	227.38	68.324	136.37	2161
Weak crust	29.289	0.17925	17.566	278
Strong mantle	10.757	3219.3	30.836	156
Weak mantle	1.0757	1.2816	3.0836	16

Crust has Young's modulus of 5.0 x 10^{10} Pa, mantle has Young's modulus of 1.6 x 10^{11} Pa; crust has Poisson's ratio of 0.25, mantle has Poisson's ratio of 0.28; crust has power law exponent of 2.9, mantle has power law exponent of 3.4; crust has rigidity of 2.0 x 10^{10} Pa, mantle has rigidity of 6.25 x 10^{10} Pa.

Table 5. Parameters for Thrust Fault of Finite Element Models

Depth, km	Distance, km	n	η_{eff} Pa s	T_m, years
Deep Coupling on Thrust Fault				
0-7.5	0-25	5.0	4.4621 x 10^{18}	3.5
7.5-13	25-50	5.0	2.6442 x 10^{19}	20.9
13-19.5	50-75	5.0	4.7926 x 10^{19}	38.0
19.5-26	75-100	5.0	6.9410 x 10^{19}	55.0
26-33.5	100-125	5.0	9.0894 x 10^{19}	72.0
33.5-41	125-150	5.0	1.1238 x 10^{20}	89.0
41-49.5	150-175	5.0	1.3386 x 10^{20}	106.0
49.5-58	175-200	5.0	1.5535 x 10^{20}	123.1
58-67.5	200-225	5.0	1.8179 x 10^{20}	144.0
67.5-77	225-250	5.0	1.9831 x 10^{20}	157.1
77-150	250-450	3.4	5.9832 x 10^{18}	4.7
Shallow Coupling on Thrust Fault				
0-7.5	0-25	5.0	4.4621 x 10^{18}	3.5
7.5-13	25-50	5.0	4.7926 x 10^{19}	38.0
13-19.5	50-75	5.0	1.3386 x 10^{20}	106.0
19.5-26	75-100	5.0	1.9831 x 10^{20}	157.1
26-33.5	100-125	5.0	1.3386 x 10^{20}	106.0
33.5-41	125-150	5.0	4.7926 x 10^{19}	38.0
41-77	150-175	5.0	4.4621 x 10^{18}	3.5
77-150	175-450	3.4	3.0836 x 10^{18}	2.4

n, power law exponent; η_{eff} effective viscosity; T_m, Maxwell time. For all fault elements, Young's modulus is 10^{11} Pa; Poisson's ratio is 0.25; shear modulus is 40 GPa; and density is 3000 kg/m^3.

Equation (6) was developed by *Melosh and Raefsky* [1980] for finite element work and is based on equations for the behavior of glacial ice [*Patterson*, 1981]. Laboratory work on rocks suggests that their viscous behavior may also be described by such an equation [*Kirby and McCormick*, 1990]. *Melosh* [1978] and *Williams and Richardson* [1991] show the correlation of power law rheology to the dislocation creep mechanism.

For Newtonian viscosity (n = 1), (6) reduces to $\dot{\varepsilon}_{ij} = \tfrac{1}{2}\ \sigma_{ij} / \eta_e$, in which case the viscosity coefficient $\eta_e = \eta_c = \eta_{\text{eff}}$ and is equivalent to the viscosity η with units of Pa s. As pointed out by *Patterson* [1981], as n approaches infinity, the viscous strain rate approaches zero when $\sigma_{ij} / \eta_e < 1$ and becomes infinite when $\sigma_{ij} / \eta_e > 1$. Thus a high n simulates brittle fracture with a shear yield stress equal to η_e. Elastic properties are specified by Young's modulus and Poisson's ratio. We adopt power law exponents and effective viscosities based on *Williams and Richardson* [1991] (Tables 3 to 5).

One of us (P. Zwick) developed a function library for TECTON to simulate 2-D structure with infinite length in the third dimension and a full six-component stress tensor. Velocity and stress gradients in the third dimension are constrained to be zero. This hybrid "2.5D" routine yields a fast, close approximation to the results obtained in 3-D models. Calibration runs during program development ensure consistency with analytical results as well as with earlier versions of the program. When a high Young's modulus is used to minimize elastic strains, the 2.5D model gives results that, in terms of slip vector direction at the base of the forearc, agree with analytical solutions for rigid blocks [*McCaffrey*, 1992] to the fourth decimal place for a range of power law exponents ranging from 1 to about 50. Full 3-D runs using TECTON of long, straight forearcs (trench-parallel length is ~8 times forearc width) give stresses and strain rates in the center cross section that agree with analytical and 2.5D solutions to within ~0.5%.

For Sumatra we use a simple structure of the crust and mantle (Figure 4 and Tables 3 to 5). In the wedge above the downgoing plate, the cooler "crustal" layer is warped downward to simulate

the effect of depressed temperature above the slab due to advective cooling by the subducting plate [*Peacock*, 1996]. The thrust fault at the base of the forearc is modeled as a 2-km-thick layer between the upper plate and subducting slab. We use a high exponent (n=5) in this layer to simulate plastic behavior along the fault zone. Nodes at the base of the thrust fault are constrained to move with the subducting slab at 70 mm/yr and obliquity of 40° resulting in 45 mm/yr of along arc motion and 54 mm/yr of convergence. The stress on the base of the hanging wall generated by the motion of the subducting slab beneath it is determined by the convergence velocity and the viscosity of the thin fault layer. We increase viscosity with depth in the thrust fault layer to let stress increase with depth within the shallow part of the "coupled zone". Viscosity is then reduced to a very low value at greater depth to simulate a constant coefficient of friction at shallow levels and then a decay of stress at depth due to increasing temperature (Figure 5a). The thrust fault continues past the coupled zone with very low viscosity (and hence low stress) to a depth of 155 km at a distance of 450 km from the trench. The vertical edge of the back arc 600 km from the trench is not allowed to move horizontally, while the base of the back arc in the mantle at 155 km depth cannot move vertically (Figure 4).

Effects of gravity on the model are not included directly as body forces acting on the elements. Instead, surface nodes in the forearc of the model are constrained to move in a plane that is parallel to the thrust fault directly below them. This constraint minimizes volumetric changes in the forearc due to motion across the forearc. It simulates the gravitational effects of changes in topography by allowing the development of vertical normal stresses near the surface. However, it does not model deformation that can arise from topographic gradients. Note that such topographic gradients can only form in the across-strike direction because the 2-D model does not permit velocity gradients (strain rates) along strike.

We explore the influence of plate coupling variations, mantle viscosity variations, and a weak zone in the upper plate (a "volcanic arc") with six models (Tables 3 and 4). Two variations in the downdip distributions of viscosities along the thin thrust fault elements are used to test the effects of "shallow" and "deep" coupling along the thrust plane (Table 5). Temporal and downdip

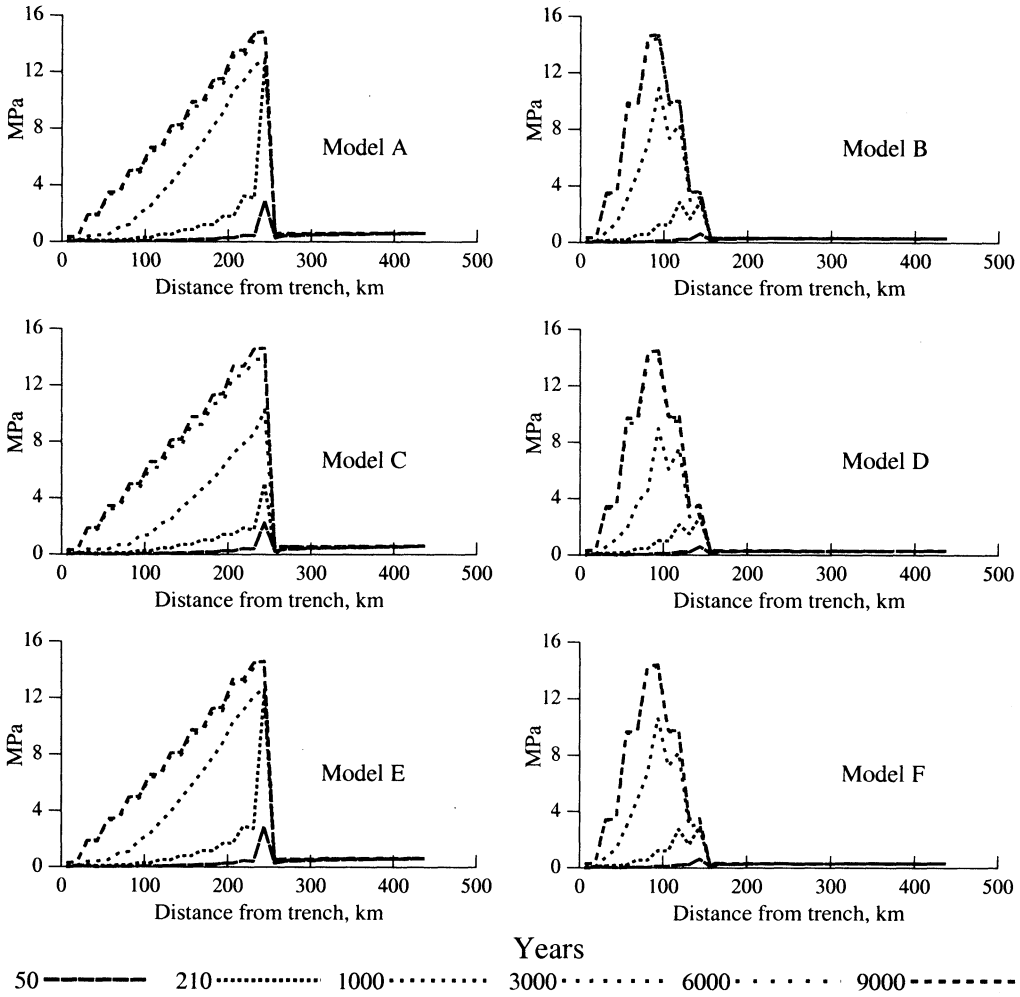

Figure 5a. Across-strike profiles of basal effective stresses for the six finite element models, shown at times of 50, 210, 1000, 3000, 6000, and 9000 years (times are designated by differing line types as shown at bottom). Basal stress and transverse velocities increase with time at short times due to the time-dependent elastic part of the deformation and then reach steady state at about 3000 years when the viscous component dominates. The basal stresses in models A and B show the difference between the shallow- and deep-coupling models. The shallow-coupling model at short times shows a steady increase in stress to about x = 150 km (depth of 41 km) and at longer times the stress becomes symmetric about x=90 km (depth of 25 km). The deep-coupling models shows an increase in stress to x=250 km (depth of 75 km) and a sharp decrease deeper where the more ductile mantle forms the upper plate.

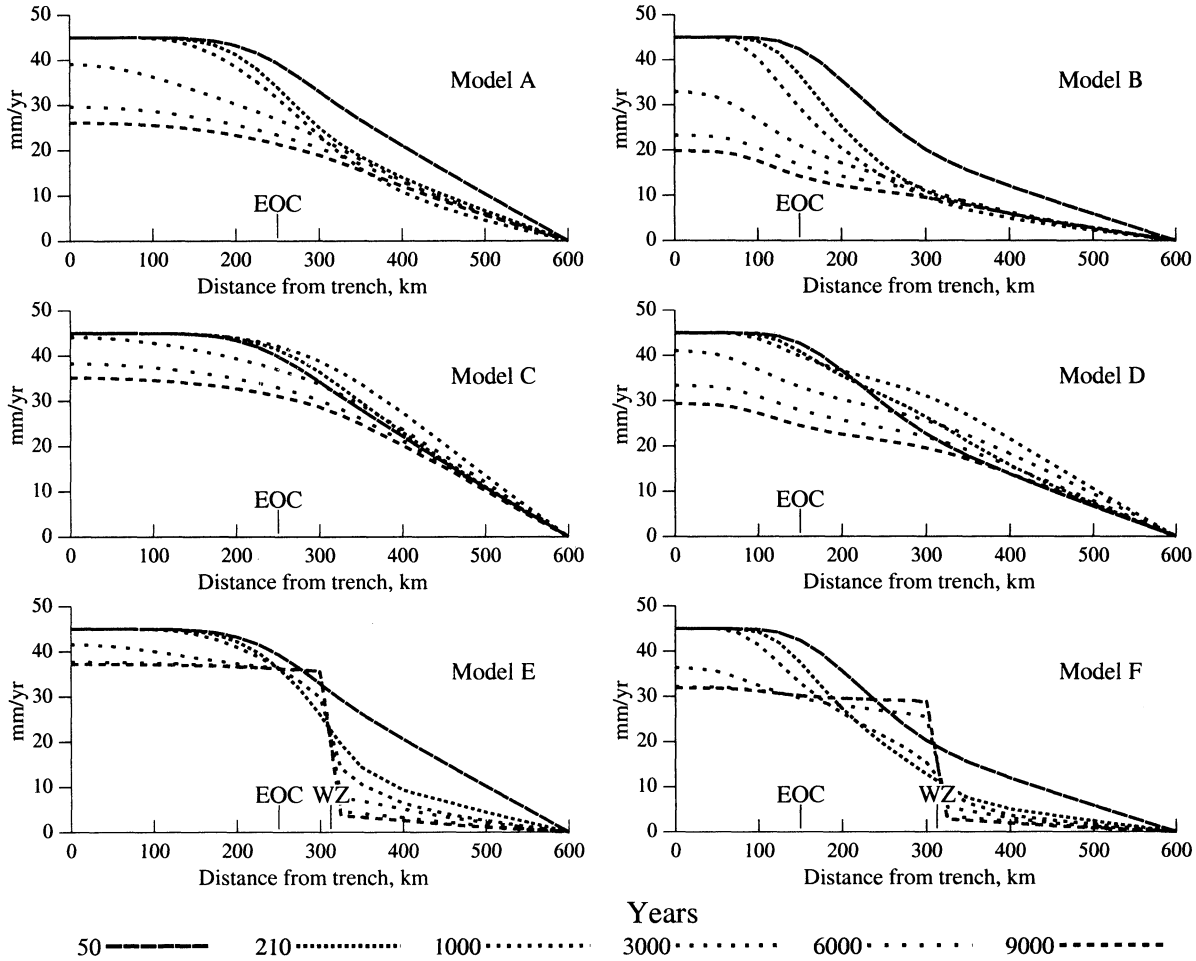

Figure 5b. Same as Figure 5a, except profiles of transverse (trench-parallel) surface velocities are shown. The label EOC shows the distance at which basal stress diminishes to near zero, and WZ represents the position of the weak zone of elements in models E and F.

variations in basal effective stress are shown in Figure 5a for the two coupling models. The shallow and deep coupling models are then run with both weak and strong mantle structures. Finally, in the final two models we place a weaker zone within the upper plate to simulate the thermal weakening effects of a volcanic arc.

We present the results for the six models for two times, 210 years and 3000 years. Although we do not model the earthquake cycle by imposing slip events and stress drops, we use the deformation pattern at 210 years as indicative of the interseismic period because it is dominated by elastic loading of the crust. The repeat time of great quakes in Sumatra is not known; in the past 300 years, there have been two great earthquakes at adjacent but not overlapping segments of the Sumatran subduction zone (both in the mid-1800s) [*Newcomb and McCann*, 1987]. At 210 years the crust has elastic behavior (T_m = 2160 years) and the strong mantle has a larger viscous component (T_m = 156 years). At 3000 years, elastic strain rates are small in all regions, and stresses and deformation rates are approaching steady state (Figure 5). We view this time as indicative of the long-term permanent deformation pattern.

Models A and B both have a strong mantle and no upper plate weak zone but differ from each other in the depth extent of the coupling. The resulting contraction in the forearc over the coupled plate interface at 210 years is perpendicular to the trench and rotates anticlockwise near the downdip end of the stressed section of the thrust fault (EOC shows the end of coupling; Figures 6a and 7a). In these models the contraction rate is low in the outer 50 km or so of the upper plate probably because the basal stresses are low at shallow depths on the thrust fault (Figure 5a). Between 50 and 100 km distance from the trench, the contraction rate increases and is nearly perpendicular to the trench. Approaching the EOC point, the contraction direction at the surface rotates anticlockwise by tens of degrees and the magnitude of the extension increases. The extension rate does not become as large as the contraction rate as in Sumatra. Nevertheless, the rotation of the contractional axis appears to be signaling the presence of the end of plate coupling beneath it. Comparing model B to model A shows that the rotation of the principal axes occurs closer to the EOC region than to the contact between the crust and mantle that intersects the fault plane at x=250 km. The increase in the margin-parallel shear strain above the EOC can also be seen in the profiles of the margin-parallel velocities (Figure 5b). We see that for most of the models and times the curves are fairly flat seaward of the EOC region and then start to slope downward in the vicinity of the EOC. The transition from purely arc-normal contraction to a notable increase in the amount of arc-parallel shear strain occurs even though a strike-slip fault is not included as a zone of weakness in models A and B. The surface strains appear to be sensitive to the distribution of stress on the dipping plate interface. Hence strain partitioning might occur even if the Sumatran fault is strong, that is, if its vertically averaged yield stress were similar to that of the surrounding rock.

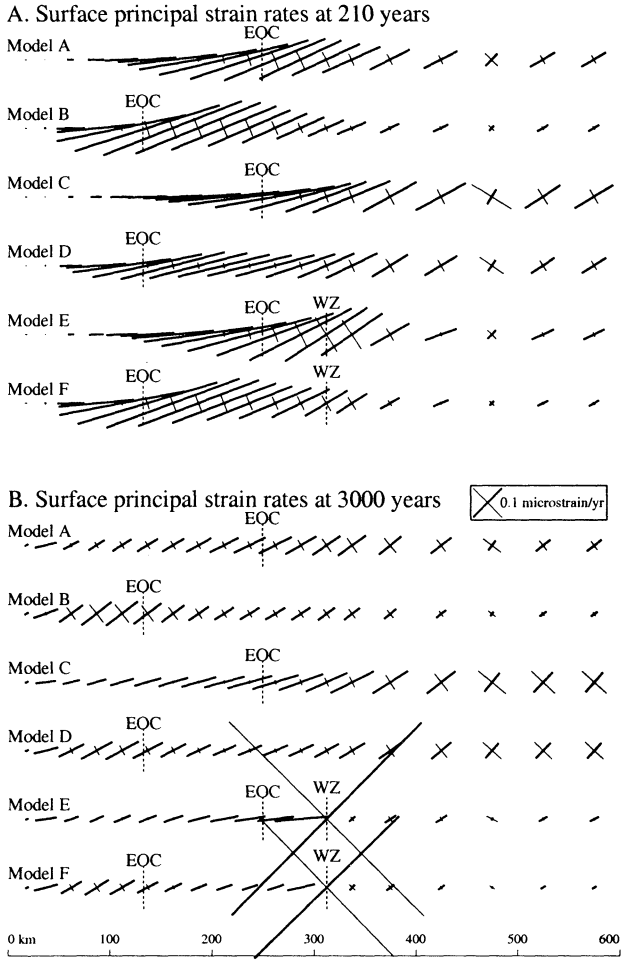

Figure 6. Map view of principal surface strain rates at (a) 210 and (b) 3000 years for the six models. Thick lines show contractions, thin lines are extension, and scale is given in box. Vertical dashed lines show the surface projection of the downdip end of interplate coupling (EOC) and the location of the weak zone (WZ) in models E and F. At short times most models show rotation of the contraction axes and growth of the extension axes away from the trench, with or without the weak elements in models E and F. This rotation occurs closer to the trench (left side) for the shallow-coupling models (B, D, and F) than for the deep-coupling models. For longer times (Figure 6b) the weak elements along the "volcanic arc" in models E and F take up most of the margin-parallel shear strain.

In models A and B that have a high-viscosity mantle, margin-parallel surface strain rates reach a maximum above the EOC and decrease landward. Models C and D are similar to models A and B except that the effective viscosity of the mantle in models C and D is decreased by a factor of 10. The effect of the lower-viscosity mantle is to spread the margin-parallel shear strain out more across the back arc. Figure 7a shows that the more viscous mantle in models A and B resists deformation and helps to localize the shear strain near the EOC, while the less viscous mantle in models C and D allows strain to be distributed across the back arc. Still the shear strain is low over the region seaward of the EOC. With a weak mantle and shallow coupling (model D) we continue to see a rotation of the principal strains over the downdip edge of the high coupling zone (Figure 7a).

Models E and F are similar to models A and B but have a vertical column of elements from 300 to 325 km from the trench that have been assigned lower viscosity than adjacent elements (effective viscosity is factor of 8 lower for crust and factor of 10 lower for mantle; Table 4). This localized decrease in viscosity simulates a hot zone in the crust and upper mantle along the volcanic arc. It is not obvious how much weaker the volcanic arc might be than the surrounding lithosphere, and we suggest that an order of magnitude is an extreme. In the deep coupling model E, margin-parallel shear strain quickly localizes along the weak zone, probably in part because it is near the region above the EOC where strain tends to localize even without the weak zone (compare model E to model A in Figures 6a and 7a). For the shallow-coupling model F the principal strain directions start rotating above the EOC and remain rotated landward to the upper plate weak zone (Figures 5b, 6a, and 7a).

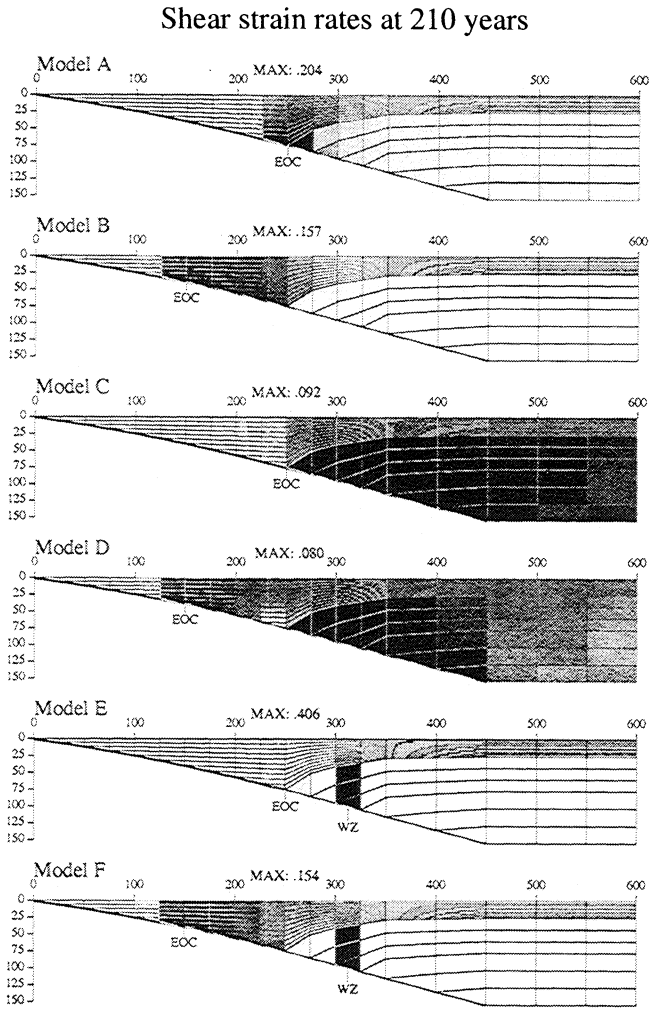

Figure 7a. Cross-section of shear strain rates across vertical planes perpendicular to the page (margin parallel shear strain) at 210 years. Darker shading indicates higher strain rates. Maximum values (MAX) are given in microstrain per year. EOC shows the location of the downdip end of interplate coupling, and WZ marks the location of the weak zone in models E and F. Strain rates are highest at the downdip edges of the thrust interface coupling regions at x=250 km for the deep-coupling models (A, C, and E), at x=125 km for shallow coupling (B, D, and F), and near the weak volcanic arc zone near x=300 km in models E and F.

In the long-term deformation, which is dominated by the viscous response of the model, the major feature that develops is margin-parallel shear strain localization at the weak zone in the crust and mantle for both the deep- and shallow-coupling models (models E and F; Figures 5b, 6b, and 7b). The overall strain rates in the forearc are smaller than in the short term due to cessation of elastic strain increase, but still the EOC region appears to be accompanied by a rotation of the principal axes and some increase in the extension rates (Figure 6b). In models E and F, high shear strain rates at the weak zone reduce the amount of strain that is required in the forearc and back arc regions. The small amounts of long-term localization of shear strain above the EOC in models A through D might result in further strain localization by reduction in strength through the generation of faults [*Buck and Poliakov*, 1998]. This weakening would then lead to an evolution of the system similar to that in models E and F except that the high strain regions would be spatially controlled by the EOC instead of by a preexisting weak zone or volcanic arc. Even model F, with a weak zone and shallow coupling, shows a local increase in margin-parallel shear strain above the EOC for as long as 6000 years (Figure 5b). Such models suggest that in regions of oblique convergence, even in the absence of a volcanic arc, the localization of margin-parallel shear strain and the development of trench-parallel strike-slip faults may be controlled by the downdip distribution of stress on the dipping plate interface. However, as such systems evolve through time and strike-slip faults form, the downdip end of coupling may produce a less obvious shear zone in the upper plate seaward of the major, fault-controlled shear.

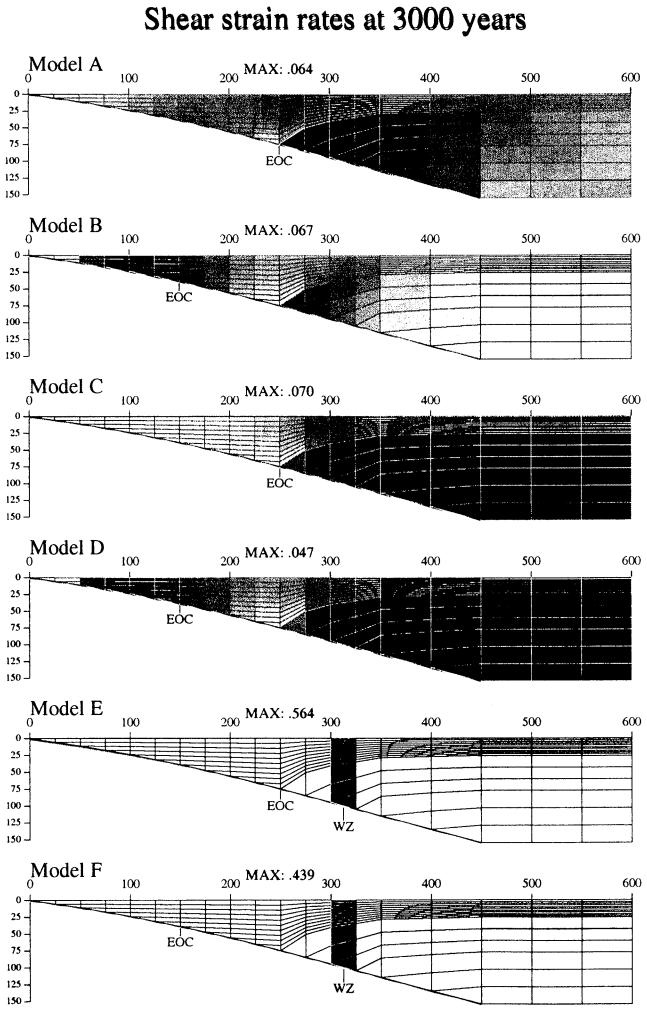

Figure 7b. Same as Figure 7a, except at 3000 years.

We can also compare the observed interplate slip vector directions to those predicted by the models. Slip vectors complement the surface geodetic data because they provide information about deformation rates at the base of the forearc. Slip vectors are calculated from the model by subtracting the velocities of the overriding plate just above the fault zone (nodes at the top of the thin "fault zone") from the velocities of the downgoing plate (the bottom nodes). Figure 8 shows the predicted slip vector directions for the six models at 210 and 3000 years compared to observed slip vectors from the Sumatran forearc. The observed slip vectors rotate from being nearly trench-normal at the trench to being nearly parallel to the convergence direction within a distance of 200 km from the trench. As pointed out earlier, this slip vector rotation can be explained by roughly 2/3 of the margin-parallel slip occurring on the Sumatran fault and roughly 1/3 of it between the forearc islands and the trench.

The FEM models that do the best job of predicting this short-scale rotation of slip vectors at 210 years are models B and F (and model D to some degree) (Figure 8a); these models have only shallow coupling on the thrust fault (Figure 5a). It appears then from the across-arc rotation of the slip vectors that the downdip end of the strong interplate coupling could occur at ~125 km from the trench. *Newcomb and McCann* [1987] used a value for the landward extent of rupture in the 1833 and 1861 great subduction events of 100 km from the trench noting that the 1861 event produced a large tsunami on the SW coast of Nias, suggesting a large amount of rupture between Nias and the trench. *Zachariasen et al.* [1999] place the end of coseismic slip during the 1833 event at a distance of ~170 km from the trench on the basis of dislocation modeling of coseismic coral emergence in the outer forearc islands. Interplate quakes presently occur farther landward, reaching 200 km from the trench (Figure 2), indicating that there is some level of stress and stick-slip behavior on the plate boundary this far from the trench. It is probable that the magnitude of the stress on the thrust fault between the forearc islands and the coast of Sumatra is lower than that below and seaward of the forearc islands.

5. Discussion

Dislocation models suggest that during oblique subduction, margin-parallel shear will concentrate in the upper plate roughly above the downdip limit of plate coupling [*Savage*, 1983]. If zones of weakness are present in the overriding plate near this region of increased shear stress, then such zones may serve to localize the shear strain and form faults. The factors that govern where the upper plate will ultimately fail include how rapidly the shear stress decays spatially away from the highest stress region, the orientations and locations of the preexisting planes of weaknesses, and the yield stresses on such weak planes. In nature, these factors are probably impossible to evaluate with much confidence. Nevertheless, to the degree that the Earth, at the scale of overriding plates at subduction zones, is sufficiently heterogeneous that it approaches a continuum, we might expect to see margin-parallel strike-slip faults forming generally above the downdip limit of the largest interplate stress.

An alternative explanation is that forearc slivers detach from the upper plate along the weak volcanic arc independently of the landward extent of coupling on the dipping plate boundary [*Beck*, 1983]. Some examples of strike-slip faults passing through or

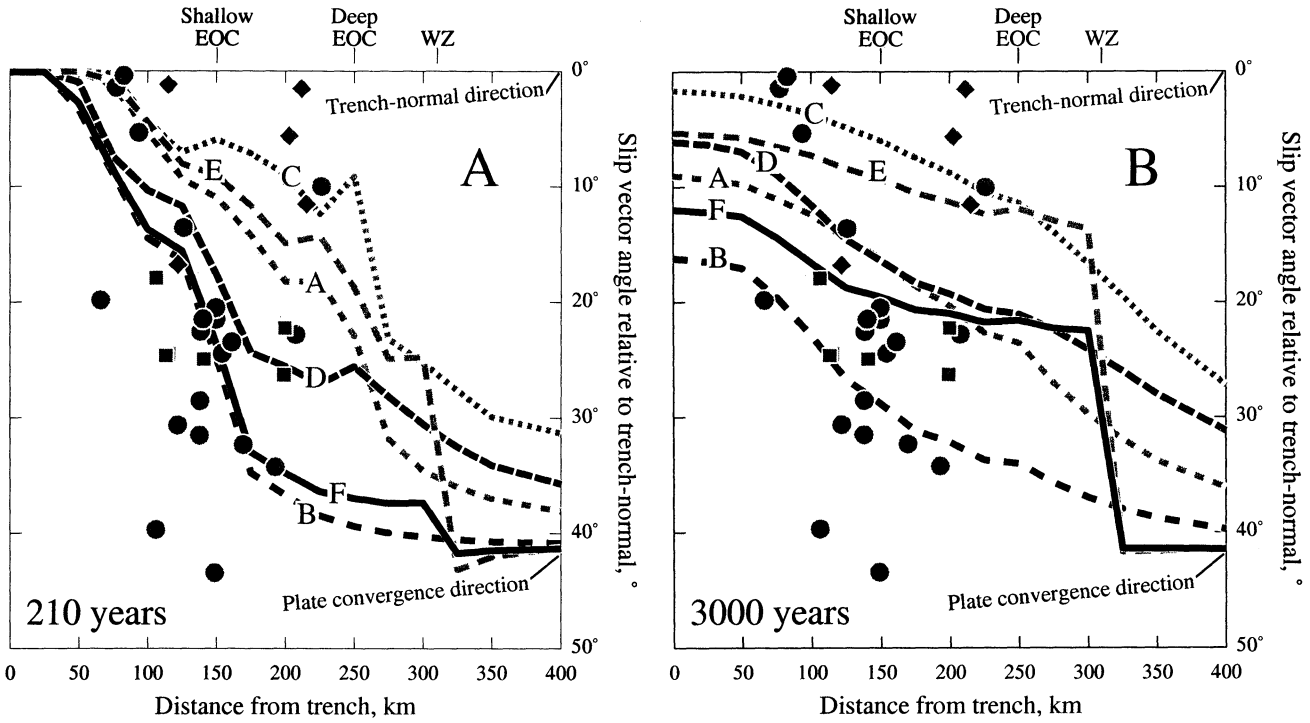

Figure 8. Profiles across the forearc showing the predicted slip vector directions at (a) 210 and (b) 3000 years. Curves are labeled by the model letter, and shaded curves correspond to the deep-coupling models (A, C, and E). Observed slip vectors are plotted relative to the trench-normal direction; dots from segment A, squares from segment B, and diamonds from segment C. EOC shows the location of the downdip end of interplate coupling for the shallow- and deep-coupling models, and WZ marks the location of the weak zone in models E and F. The rapid rotation of the slip vectors landward from the trench appears to be matched better by the shallow-coupling models.

close to the volcanic arc are the Sumatran fault, the Philippine fault [*Barrier et al.*, 1991], the Liquine-Ofqui fault in southern Chile, and the Guayanquil fault in Ecuador and Colombia.

However, narrow sliver plates in oblique subduction zones with bounding strike-slip faults that cut through the forearc seaward of the volcanic arc are equally common. In the Aleutians the Hawley Ridge fault parallels the trench ~50 km landward of it and appears to detach a westward moving forearc sliver [*Scholl*, 1999]. Similar faults are found along the southern Ryukyu arc [*Lallemand and Chemenda*, 1999] and north of Puerto Rico [*Grindlay et al.*, 1999]. The Atacama fault in northern Chile falls about halfway between the trench and the volcanic arc. Inferences of thin forearc slivers have also been made for the San Cristobal and northern Tonga trenches based on observations of slip vector deflections [*McCaffrey*, 1996b].

The location of the upper plate strike-slip faults in all these cases could be arising from the downdip distribution of interplate coupling stress. By careful study of earthquake depths at 13 selected subduction zone segments, *Tichelaar and Ruff* [1993] found that the downdip limit of seismic slip ranges generally from 40 to 50 km depth, with the exceptions of Mexico at 20-25 km and Hokkaido at 55 km. *Pacheco et al.* [1993] studied 23 subduction zone segments using the less reliable centroid depths from the routine Harvard centroid moment tensor solutions and found the downdip limit ranging from 33 to 70 km, but most were in the 40 to 50 km range (three were <40 km and four were >50 km). Because subducting plates dip below trenches at a very low angle and then steepen as they approach the volcanic arc, the 40- and 50-km depth contours of the top of the slab, in map view, will be closer to the volcanic arc than to the trench. For example, *Ruff and Tichelaar* [1996] measured the horizontal distances between the trench and the landward end of interplate seismic slip and between the trench and the volcanic arc for their 13 subduction segments. Their average trench-to-arc distance is 270 km, and the average trench-to-edge of coupling distance is 170 km. Hence the downdip edge of plate coupling generally comes within 100 km of the volcanic arc, which we suggest is in some cases sufficiently close to localize shear on a fault cutting through the arc. In Sumatra the seismogenic section of the subduction thrust fault comes to within 50 km of the volcanic arc (Figure 2) although it appears that the larger stress occurs on the outer half of the thrust fault.

Arc-parallel shear in the Sumatran forearc may be taken up on more than one strike-slip fault or shear zone, as suggested by *Diament et al.* [1992], although we disagree with them that the 10-15 mm/yr of missing strike-slip from the Sumatran fault occurs on the Mentawi fault [see also *Genrich et al.*, this issue]. The trace of the Mentawi fault, as mapped by *Diament et al.* [1992], is along the landward edge of the forearc islands south of Nias and then comes on land on Nias. The GPS network crosses the northern third of the Mentawi fault, and we see no clear indications of large transverse motions [*Genrich et al.*, this issue]. Where the Mentawi fault comes on land on Nias, it is interpreted to be a reverse fault [*Samuel and Harbury*, 1996].

Instead, the obliquity of the slip vectors beneath and landward of the forearc islands suggests that there is considerable margin-parallel shear strain in the forearc seaward of the forearc islands (and seaward of the geodetic network). If our inference that this

shear strain is caused by high interplate coupling seaward of the forearc islands is correct, then this suggests that it might be possible to assess stress distributions on dipping plate boundaries in regions of oblique convergence even when the upper plate shear strain is dominated by a major strike-slip fault. While we are unable to measure the strain seaward of the Sumatran forearc islands with geodetic methods, some subduction zones allow more dense spatial coverage and greater proximity to the trench or the strain may occur farther from the trench in more accessible regions.

Most subduction and convergent margins are convex toward the downgoing plate, and many reveal margin-parallel stretching [*Ekström and Engdahl*, 1989; *McCaffrey* 1992, 1996a]. Such margin-parallel stretching occurs in the Sumatran forearc as well (Figure 2). From the numerical results above, we can make inferences about the relationship of the stretching regions to the coupled plate interface. Specifically, in the case of a curved, convex-seaward subduction zone it is likely that the upper plate margin-parallel extension occurs over, and therefore reveals, the region of interplate coupling. In the 2-D numerical models, margin-parallel shear strain is seen to increase above the downdip edge of plate coupling. Seaward of the upper plate shear zone the forearc moves rapidly relative to the back arc (e.g., Figure 5b) and is driven by the basal shear of the dipping plate boundary. As the convergence obliquity increases along strike of a curved margin, the rate of forearc motion relative to the rest of the overriding plate may also increase because obliquity largely controls the fraction of the margin-parallel component of forearc motion (Figure 3a). Hence margin-parallel gradients in the margin-parallel velocity (i.e., along–strike extensional strain) in the forearc will be largest over the coupled plate boundary where the basal driving forces are acting. This process can be shown with a simple experiment using blocks arranged on the perimeter of a moving, curved board [*Avé Lallemant and Guth*, 1990; *McCaffrey and Nabelek*, 1998]. The basal drag on the blocks and the curvature of the backstop cause the blocks to move laterally along the curved edge and to separate as they are pushed along.

Accordingly, there should be a spatial correlation between interplate coupling and forearc extensional deformation. In the Aleutians the forearc deformation occurs without a clear strike-slip fault along the volcanic arc [*Geist et al.*, 1988] despite oblique convergence in the Aleutians being strongly partitioned [*Ekström and Engdahl*, 1989; *McCaffrey*, 1992]. Interplate thrust earthquakes occur only beneath the deforming forearc region [*Tichelaar and Ruff*, 1993]. In the Oregon segment of Cascadia, where there are no interplate earthquakes, the plate coupling is thought to be largely offshore [*Hyndman and Wang*, 1995], where the most obvious upper plate deformation is located [*Goldfinger et al.*, 1992]. In the Himalayas and southern Tibet, active normal faulting extends the upper plate parallel to the deformation front. The normal faults continue at least 500 km north of the deformation front where they are largely, but not completely, truncated by a set of E-W striking strike-slip faults, called the Karakorum–Jiali fault zone (KJFZ) [*Armijo et al.*, 1986, 1989]. Interplate thrust earthquakes extend only to about 150 km north of the deformation front [*Molnar and Lyon-Caen*, 1989], yet seismic data suggest that the Indian lithosphere extends beneath southern Tibet as far north as the KJFZ [*Owens and Zandt*, 1997]. The modeling presented in this paper supports the notion that the extension and shear deformation in southern Tibet and the Himalayas could be driven by basal shear of India sliding obliquely beneath it [*McCaffrey and Nabelek*, 1998] as an alternative mechanism to gravitational collapse of an overly thickened lithosphere [*England and Houseman*, 1989].

6. Conclusions

GPS results from northern Sumatra show that upper plate strain associated with the oblique convergence there is partitioned into trench-normal contraction across the forearc and trench-parallel shear strains within a few tens of kilometers of the volcanic arc. Earthquake slip vectors, used to infer that strain partitioning is quite common at subduction zones and other convergent margins, are shown to be reliable indicators of the kinematics of slip partitioning. GPS and slip vectors together suggest that about two-thirds of the margin-parallel component of relative plate motion in northern Sumatra occurs on the Sumatran fault and a third occurs in the forearc seaward of the forearc islands. Numerical models demonstrate that a preexisting zone of weakness within the overriding plate, such as a strike-slip fault or volcanic arc, is not necessary for strain partitioning to develop, although they can enhance it or localize the strike-slip component. The downdip distribution of stress on the subduction thrust alone can cause the stresses in the overriding plate that lead to strain partitioning. In fact, strain partitioning that occurs initially due to oblique subduction may determine where the strike-slip fault eventually develops within the overriding plate. Accordingly, not all margin-parallel strike-slip faults need occur at the volcanic arc. Finally, geodetically measured contemporary margin-parallel shear strains in the overriding plates at oblique subduction zones can be useful in outlining the distribution of shear stresses on dipping thrust plate boundaries.

Acknowledgments. We thank Jay Melosh for allowing use of the FEM program TECTON. Helpful reviews were supplied by Tim Dixon, Jeanne Sauber, Paul Lundgren, Peter Morgan, and Charles Williams. This study was supported by grants to RPI (NSF EAR-8908759 and EAR-9114349) and SIO (NSF EAR-8817067 and EAR9114864 and NASA NAGW-2641) and by the Indonesian government.

References

Armijo, R., P. Tapponnier, J. L. Mercier, and T. L. Han, Quaternary extension in southern Tibet: Field observations and tectonic implications, *J. Geophys. Res., 91*, 13803-13872, 1986.

Armijo, R., P. Tapponnier, and H. Tonglin, Late Cenozoic right-lateral strike-slip faulting in southern Tibet, *J. Geophys. Res., 94*, 2787-2838, 1989.

Avé Lallemant, H. G., and L. R. Guth, Role of extensional tectonics in exhumation of eclogites and blueschists in an oblique subduction setting, northwest Venezuela, *Geology, 18*, 950-953, 1990.

Barrier, E., P. Huchon, and M. Aurelio, Philippine Fault: A key for Philippine kinematics, *Geology, 19*, 32-35, 1991.

Beck, M. E., On the mechanism of tectonic transport in zones of oblique subduction, *Tectonophysics, 93*, 1-11, 1983.

Bock, Y., R. McCaffrey, J. Rais, and I. Murata, Geodetic studies of oblique plate convergence in Sumatra, *Eos Trans. AGU, 71*, 857, 1990.

Buck, W. R., and A. N. B. Poliakov, Abyssal hills formed by stretching oceanic lithosphere, *Nature, 392*, 272-275, 1998.

DeMets, C., R. G. Gordon, D. F. Argus, and S. Stein, Effects of recent revisions to the geomagnetic reversal time scale on estimates of current plate motions, *Geophys. Res. Lett., 21*, 2191-2194, 1994.

Diament, M., H. Harjono, K. Karta, C. Deplus, D. Dahrin, M. T. Zen Jr, M. Gerard, O. Lassal, A. Martin, and J. Malod, Mentawai fault zone off Sumatra: a new key to the geodynamics of western Indonesia, *Geology, 20*, 259-262, 1992.

Douglass, J. J., and B. A. Buffett, The stress state implied by dislocation models of subduction deformation, *Geophys. Res. Lett., 22*, 3115-3118, 1995.

Dziewonski, A. M., T.-A. Chou, and J. H. Woodhouse, Determination of earthquake source parameters from waveform data for studies of global and regional seismicity, *J. Geophys. Res., 86*, 2825-2852, 1981.

Ekström, G., and E. R Engdahl, Earthquake source parameters and stress distribution in the Adak Island region of the central Aleutian Islands, Alaska, *J. Geophys. Res., 94*, 15,499-15,519, 1989.

Ekström, G. and M. Nettles, Calibration of the HGLP seismograph network and centroid-moment tensor analysis of significant earthquakes of 1976, *Phys. Earth Planet. Inter., 101,* 221-246, 1997.

England, P., and G. Houseman, Extension during continental convergence, with application to the Tibetan Plateau, *J. Geophys. Res., 94,* 17,561-17,579, 1989.

Fauzi, R. McCaffrey, D. Wark, Sunarjo, and P. Y. Prih Haryadi, Lateral variation in slab orientation beneath Toba caldera, northern Sumatra, *Geophys. Res. Lett., 23,* 443-446, 1996.

Feigl, K. L., et al., Measurement of the velocity field of central and southern California, 1984-1992, *J. Geophys. Res., 98,* 21,677-21,712, 1993.

Fitch, T. J., Plate convergence, transcurrent faults, and internal deformation adjacent to southeast Asia and the western Pacific, *J. Geophys. Res., 84,* 4432-4460, 1972.

Geist, E. L., J. R. Childs, and D. W. Scholl, The origin of summit basins of the Aleutian Ridge: Implications for block rotation of an arc massif, *Tectonics, 7,* 327-341, 1988.

Genrich, J. F., Y. Bock, R. McCaffrey, L. Prawirodirdjo, C. W. Stevens, S. S. O. Puntodewo, C. Subarya, and S. Wdowinski, Distribution of slip at the northern Sumatra fault system, *J. Geophys. Res.*, this issue.

Goldfinger, C., L. D. Kulm, R. S. Yeats, B. Appelgate, M. MacKay, and G. F. Moore, Transverse structural trends along the Oregon convergent margin: Implications for Cascadia earthquake potential, *Geology, 20,* 141-144, 1992.

Grindlay, N. R., P. Mann, and J. Dolan, Oblique collision of the Bahama Platform in the Hispaniola–Puerto Rico area, northeastern Caribbean, paper presented at Penrose Conference on Subduction to Strike-slip Transitions on Plate Boundaries, Geological Society of America, Puerta Plata, Dominican Republic, 1999.

Hyndman, R. D., and K. Wang, The rupture zone of Cascadia great earthquakes from current deformation and the thermal regime, *J. Geophys. Res., 100,* 22,133-22,154, 1995.

Jarrard, R. D., Relations among subduction parameters, *Rev. Geophys., 24,* 217-284, 1986.

Katili, J. A., and F. Hehuwat, On the occurrence of large transcurrent faults in Sumatra, Indonesia, *J. Geosci., 10,* 5-17, 1967.

Kirby, S. H., and J. W. McCormick, Inelastic properties of rocks and minerals: strength and rheology, *Practical Handbook of Physical Properties of Rocks and Minerals,* CRC Press, edited by R. S. Carmichael, pp. 177-297, Boca Raton Fla., 1990.

Lallemand, S., and A. Chemenda, Strain partitioning and coupling between plates: Field observations and critical input from experimental modeling, paper presented at Penrose Conference on Subduction to Strike-slip Transitions on Plate Boundaries, Geological Society of America, Puerta Plata, Dominican Republic, 1999.

Larson, K. M., J. T. Freymueller, and S. Philipsen, Global plate velocities from the Global Positioning System, *J. Geophys. Res. 102,* 9961-9981, 1997

Liu, X., K. C. McNally, and Z.-K. Shen, Evidence for a role in the downgoing slab in earthquake slip partitioning at oblique subduction zones, *J. Geophys. Res., 100,* 15,351-15,372, 1995.

McCaffrey, R., Slip vectors and stretching of the Sumatran fore arc, *Geology, 19,* 881-884, 1991.

McCaffrey, R., Oblique plate convergence, slip vectors, and forearc deformation, *J. Geophys. Res., 97,* 8905-8915, 1992.

McCaffrey, R., Global variability in subduction thrust zone-forearc systems, *Pure Appl. Geophys., 141,* 173-224, 1994.

McCaffrey, R., Estimates of modern arc-parallel strain rates in fore arcs, *Geology, 24,* 27-30, 1996a.

McCaffrey, R., Slip partitioning at convergent plate boundaries of SE Asia, in Tectonic Evolution of Southeast Asia, edited by R. Hall and D. J. Blundell, *Geol. Soc. Spec. Publ., 106,* 3-18, 1996.

McCaffrey, R., and J. Nabelek, Role of oblique convergence in the active deformation of southern Tibet, *Geology, 26,* 691-694, 1998.

McCaffrey, R., Y. Bock and J. Rais, Crustal deformation and oblique plate convergence in Sumatra, *Eos Trans. AGU, 71,* 637, 1990.

Melosh, H. J., Dynamic support of the outer rise, *Geophy. Res. Lett., 5,* 321-324, 1978.

Melosh, H. J., and A. Raefsky, The dynamic origin of subduction zone topography, *Geophy, J. R. Astron. Soc., 60,* 333-354, 1980.

Molnar, P., and H. Lyon-Caen, Fault plane solutions of earthquakes and active tectonics of the Tibetan Plateau and its margins, *Geophys. J. Int., 99,* 123-153, 1989.

Newcomb, K. R., and W. R. McCann, Seismic history and seismotectonics of the Sunda Arc, *J. Geophys. Res., 92,* 421-439, 1987.

Owens, T. J., and G. Zandt, Implications of crustal property variations for models of Tibetan plateau evolution, *Nature 387,* 37-43, 1997.

Pacheco, J. F., L. R. Sykes, and C. H. Scholz, Nature of seismic coupling along simple plate boundaries of the subduction type, *J. Geophys. Res., 98,* 14,133-14,159, 1993.

Page, B. G. N., J. D. Bennett, N. R. Cameron, D. M. Bridge, D. H. Jeffery, W. Keats, and J. Thaib, A review of the main structural and magmatic features of northern Sumatra, *J. Geol. Soc. London, 136,* 569-579, 1979.

Patterson, W. S. B., *The Physics of Glaciers,* 2nd edition, Pergamon Press, Tarrytown, N.Y., 1981.

Peacock, S. M., Thermal and petrologic structure of subduction zones, in *Subduction: Top to Bottom,* edited by G. E. Bebout et al., pp. 119-133, AGU, *Geophys. Monogr. Ser.,* vol. 96, 119-133, Washington, D. C., 1996.

Platt, J. P., Mechanics of oblique convergence, *J. Geophys. Res., 98,* 16,239-16,256, 1993.

Prawirodirdjo, L., et al., Geodetic observations of interseismic strain segmentation at the Sumatra subduction zone, *Geophys. Res. Lett., 24,* 2601-2604, 1997.

Prawirodirdjo, L., Y. Bock, J. F. Genrich, S.S.O. Puntodewo, J. Rais, C. Subarya, and S. Sutisna, One century of tectonic deformation along the Sumatran fault from triangulation and Global Positioning System surveys, *J. Geophys. Res.*, this issue.

Ruff, L. J., and B. W. Tichelaar, What controls the seismogenic plate interface at subduction zones?, in *Subduction: Top to Bottom,* edited by G. E. Bebout et al., pp. 119-133, AGU, *Geophys. Monogr. Ser.,* vol. 96, 105-111, Washington, D. C., 1996.

Samuel, M. A., and N. A. Harbury, The Mentawi fault zone and deformation of the Sumatran fore arc in the Nias area, in Tectonic Evolution of Southeast Asia, edited by R. Hall and D. J. Blundell, *Geol. Soc. Spec. Publ., 106,* 337-351, 1996.

Sauber, J., S. McClusky, and R. W. King, Relation of ongoing deformation rates to the subduction zone process in southern Alaska, *Geophys. Res. Lett., 24,* 2853-2856, 1997.

Savage, J. C., A dislocation model of strain accumulation and release at a subduction zone, *J. Geophys. Res., 88,* 4984-4996, 1983.

Savage J. C., and M. Lisowski, Deformation in the Yakayaga seismic gap, southern Alaska, 1980-1986, *J. Geophys. Res., 93,* 4731-4744, 1988.

Scholl, D. W., East to west transition from orthogonal to oblique, to strike-slip, to orthogonal subduction along the northern rim of the Pacific Basin, paper presented at Penrose Conference on Subduction to Strike-slip Transitions on Plate Boundaries, Geological Society of America, Puerta Plata, Dominican Republic, 1999.

Sieh, K., and D. Natawidjaja, Neotectonics of the Sumatran fault, Indonesia, *J. Geophys. Res.*, this issue.

Sieh, K., J. Zachariasen, Y. Bock, L. Edwards, F. Taylor, and P. Gans, Active tectonics of Sumatra, *Geol. Soc. Am. Abstr. Programs, 26,* A-382, 1994.

Taylor, M. A. J., R. Dmowska, and J. R. Rice, Upper plate stressing and seismicity in the subduction earthquake cycle, *J. Geophys. Res., 103,* 24,523-24,542, 1998.

Tichelaar, B. W., and L. J. Ruff, Depth of seismic coupling along subduction zones, *J. Geophys. Res., 98,* 2017-2037, 1993.

Walcott, R. I., Geodetic strains and large earthquakes in the axial tectonic belt of North Island, New Zealand, *J. Geophys. Res., 83,* 4419-4429, 1978.

Wang, K. L., H. Dragert, and H. J. Melosh, Finite-element study of uplift and strain across Vancouver-Island, *Can. J. Earth Sci., 31,* 1510-1522, 1994.

Williams, C. A., and R. A. Richardson, A rheological layered three-dimensional model of the San Andreas Fault in central and southern California, *J. Geophys. Res., 96,* 16,597-16,623, 1991.

Zachariasen, J., K. Sieh, F. W. Taylor, R. L. Edwards, and W. S. Hantoro, Submergence and uplift associated with the giant 1833 Sumatran subduction earthquake: Evidence from coral microatolls, *J. Geophys. Res., 104,* 895-919, 1999.

Y. Bock, J. F. Genrich, and L. Prawirodirdjo, Institute of Geophysics and Planetary Physics, Scripps Institution of Oceanography, 9500 Gilman Drive, La Jolla, CA 92093-0225. (ybock@ucsd.edu; jeff@josh.ucsd.edu; linette@josh.ucsd.edu)

R. McCaffrey, C. W. Stevens, and P. Zwick, Department of Earth and Environmental Sciences, Rensselaer Polytechnic Institute, Troy, NY 12180-3590. (mccafr@rpi.edu)

S. S. O. Puntodewo and C. Subarya, National Coordination Agency for Surveying and Mapping, Jl. Raya Jakarta Bogor km 46, Cibinong, Indonesia. (geodesi@server.indo.net)

(Received April 19, 1999; revised September 7, 1999;
accepted October 8, 1999.)